

Geophysical Research Letters®

RESEARCH LETTER

10.1029/2021GL095090

Key Points:

- We report the concurrent observations of Pc1 wave, proton precipitation, ionospheric perturbation, field-aligned current, and isolated proton aurora (IPA)
- Pc1 waves over the ionospheric F-layer and IPA over the E-layer show different latitudinal widths
- Proton precipitation can cause localized plasma density enhancement, which is occasionally surrounded by wide/shallow density depletion

Supporting Information:

Supporting Information may be found in the online version of this article.

Correspondence to:

H. Kim,
hkim82@alaska.edu







Citation:

Kim, H., Shiokawa, K., Park, J., Miyoshi, Y., Miyashita, Y., Stolle, C., et al. (2021). Isolated proton aurora driven by EMIC Pc1 wave: PWING, Swarm, and NOAA POES multi-instrument observations. *Geophysical Research Letters*, 48, e2021GL095090. <https://doi.org/10.1029/2021GL095090>

Received 7 JUL 2021
Accepted 26 AUG 2021
Corrected 1 OCT 2021

This article was corrected on 1 OCT 2021. See the end of the full text for details.

Isolated Proton Aurora Driven by EMIC Pc1 Wave: PWING, Swarm, and NOAA POES Multi-Instrument Observations

Hyangpyo Kim^{1,2} , Kazuo Shiokawa¹ , Jaeheung Park^{3,4} , Yoshizumi Miyoshi¹ , Yukinaga Miyashita^{3,4} , Claudia Stolle⁵ , Hyunju Kim Connor² , Junga Hwang^{3,4} , Stephan Buchert⁶ , Hyuck-Jin Kwon⁷ , Satoko Nakamura¹, Kohki Nakamura¹ , Shin-Ichiro Oyama^{1,8} , Yuichi Otsuka¹ , Tsutomu Nagatsuma⁹ , and Kaori Sakaguchi⁹ 

¹Institute for Space-Earth Environmental Research, Nagoya University, Nagoya, Japan, ²Geophysical Institute, University of Alaska, Fairbanks, AK, USA, ³Korea Astronomy and Space Science Institute, Daejeon, South Korea, ⁴Korea University of Science and Technology, Daejeon, South Korea, ⁵GFZ German Research Centre for Geosciences, Potsdam, Germany, ⁶Swedish Institute of Space Physics, Uppsala, Sweden, ⁷Korea Polar Research Institute, Incheon, South Korea, ⁸National Institute of Polar Research, Tachikawa, Japan, ⁹National Institute of Information and Communications Technology, Tokyo, Japan

Abstract We report the concurrent observations of F-region plasma changes and field-aligned currents (FACs) above isolated proton auroras (IPAs) associated with electromagnetic ion cyclotron Pc1 waves. Key events on March 19, 2020 and September 12, 2018 show that ground magnetometers and all-sky imagers detected concurrent Pc1 wave and IPA, during which NOAA POES observed precipitating energetic protons. In the ionospheric F-layer above the IPA zone, the Swarm satellites observed transverse Pc1 waves, which span wider latitudes than IPA. Around IPA, Swarm also detected the bipolar FAC and localized plasma density enhancement, which is occasionally surrounded by wide/shallow depletion. This indicates that wave-induced proton precipitation contributes to the energy transfer from the magnetosphere to the ionosphere.

Plain Language Summary Electromagnetic ion cyclotron (EMIC) wave is known to precipitate energetic protons into the Earth's atmosphere via pitch angle scattering. Observations from ground-based magnetometers, all-sky imagers, and low Earth orbit satellites have shown that the precipitating protons scattered by EMIC waves can generate proton aurora isolated at a subauroral latitude. This kind of aurora is called isolated proton aurora (IPA, or detached proton auroral arc). In the present paper, we report the observations of concurrent Pc1 wave, proton precipitation, ionospheric perturbation, field-aligned currents (FACs), and IPA using data from ground instruments, and from the Swarm and NOAA POES satellites. The observations show that the latitudinal (L-shell) size of EMIC wave at Swarm altitude is larger than that of the IPA. We also investigated the effects of proton precipitation on the ionospheric F-layer from Swarm satellite data, and found localized plasma density enhancement and FAC near the central IPA region. Our results demonstrate that the EMIC-driven proton precipitation contributes to the energy transfer from the magnetosphere to the ionosphere.

1. Introduction

Electromagnetic ion cyclotron (EMIC) Pc1 waves have been known to precipitate energetic protons (Cornwall et al., 1970; Erlandson & Ukhorskiy, 2001; Jordanova et al., 2001) and relativistic electrons (Miyoshi et al., 2008; Usanova et al., 2014) into the Earth's atmosphere via pitch angle scattering induced by resonant wave-particle interactions. Observations of precipitating protons (>30 keV) associated with Pc1 wave were first reported by Yahnina et al. (2000) using data from the NOAA-12 satellite and the Sodankylä ground magnetometer. Yahnina et al. (2003) investigated energetic proton precipitation with/without lower energy (<20 keV) counterparts during Pc1 wave activity and showed that the type of Intervals of Pulsations with Diminishing Periods (IPDP) Pc1 waves is mostly accompanied by lower-energy proton precipitations. Miyoshi et al. (2008) first reported simultaneous observations of relativistic electron and energetic proton precipitations caused by the EMIC wave.

Since the launch of the Imager for Magnetopause-to-Aurora Global Exploration (IMAGE) satellite in 2000, and thus the availability of Far Ultraviolet (FUV) images with a combination of particle detections from low Earth orbit (LEO) satellites (e.g., NOAA POES, FAST, and DMSF), the detached proton aurora arcs (or isolated proton aurora, IPA, at subauroral latitudes) were suggested to be the result of proton precipitation due to the interaction with EMIC waves (Frey et al., 2004; Fuselier et al., 2004; Immel et al., 2002; Spasojevic et al., 2004; Yahnin & Yahnina, 2007; Yahnin et al., 2007). In subsequent studies, direct comparisons between IPA imaging from ground-based ASIs and concurrent Pc1 wave from ground magnetometers showed that the modulation of auroral intensity is strongly correlated with that of Pc1 waves. The results supported that the IPA is distinctly caused by EMIC-driven proton precipitation (Nakamura et al., 2021; Nomura et al., 2016; Ozaki et al., 2018; Sakaguchi et al., 2007, 2008, 2016).

Until now, observations of IPA events associated with Pc1 waves have been reported mainly from ground ASIs and magnetometers combined with observations by a single satellite. Still, direct comparison for the spatial structure of the IPA, its relation to Pc1 waves and proton precipitation, are pending. Furthermore, the behavior of F-region ionospheric plasma or field-aligned currents (FACs) due to the EMIC-driven isolated proton precipitation has neither been reported. In the present paper, we report the observations of IPA with concurrent Pc1 waves, FACs, and proton precipitation using data from the PWING (Particles and Waves in the Inner magnetosphere using Ground-based network observation) ASIs and induction magnetometers, and from the Swarm and NOAA POES satellites. We also examine the effects of proton precipitation on the ionospheric F-layer.

2. Instruments

2.1. PWING (ASI and Induction Magnetometer)

PWING, a longitudinal network of ground-based instruments at subauroral latitudes, was set up to investigate dynamics between plasma waves and particles in the inner magnetosphere. PWING ASIs take nighttime aurora images covering the auroral oval and subauroral latitudes through several different filters. To investigate the proton aurora, we used both 557.7-nm (oxygen or green line) and 486.1-nm ($H\beta$) auroral images taken with a 15-s exposure, which recorded proton aurora (486.1-nm) emitted by charge exchange of precipitating proton, and electron aurora (557.7-nm) emitted by secondary electron via proton-neutral collision. The ASI provides aurora images with a 1.5-min cadence. PWING induction magnetometers conduct induced triaxial-magnetic pulsation measurements with a 64 Hz sampling rate. Detailed information of PWING instruments is given in Shiokawa et al. (2017). We also used 20 Hz induction magnetometer data measured at King Sejong Station (KSS) in Antarctica.

2.2. LEO Satellites

Swarm is a satellite constellation placed in different polar orbits. Swarm-A and -C orbit side-by-side at an altitude of ~ 450 km (for a spherical Earth with 6,378 km radius), and Swarm-B orbits at a slightly higher altitude of ~ 505 km. The Vector Field Magnetometer measures the triaxial-geomagnetic field with a 50 Hz sampling rate, and the Langmuir Probe provides plasma density measurements at 2 Hz cadence. Swarm also provides FACs estimated from a single- and dual-satellite approach using Ampere's law under the assumption that the variations in the recorded magnetic field result from the traversal of quasi-static current sheets. Detailed method estimating FAC from dual-satellites is described in Ritter et al. (2013) and the single satellite FAC product is described in SW-TR-GFZ-GS-0005 (<https://earth.esa.int/web/guest/document-library/browse-document-library/-/article/swarm-level-2-fac-single-product-description>).

NOAA POES (hereafter NOAA) series flies on polar orbits at an altitude of ~ 800 km and detects both precipitating (field-aligned) and mirroring particles. The onboard Space Environment Monitor (SEM-2) consists of two instruments: The Medium Energy Proton and Electron Detector (MEPED) measures the fluxes of energetic protons and electrons with energies above 30 keV from solid-state telescopes, and the Total Energy Detector (TED) measures total energy fluxes of low-energy ions and electrons (< 20 keV) from the electrostatic analyzer. For more information on SEM-2, see Evans and Greer (2004).

Event 1. 19 March 2020

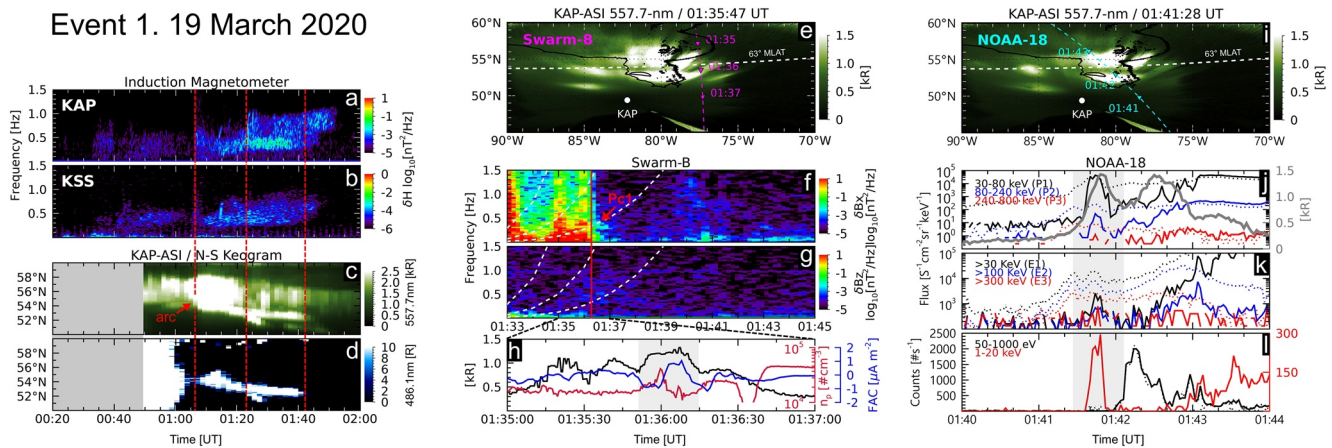


Figure 1. Stack plot of multi-instrument observations for Event 1. (a and b) Wave spectrograms of horizontal magnetic pulsation observed at Kapuskasing (KAP) and King Sejong Station (KSS), respectively (c and d) North-south keogram of 557.7 and 486.1-nm auroral emissions, respectively. (e and i) Auroral images at 01:35:47 UT and 01:41:28 UT with satellite footprints. The white dashed lines indicate 63° MLAT (f and g) Wave spectrograms of δB_x and δB_z observed by Swarm-B. The white dashed curves indicate equatorial gyrofrequencies for hydrogen, helium, and oxygen from left to right, while the red solid line indicates when Swarm-B crosses the equatorward boundary of broadband pulsations. (h) Auroral intensity (black), plasma density n_p (red), and FAC measured by Swarm-B. (j) Proton and (k) electron fluxes measured by MEPED (l) Proton count rates from Total Energy Detector (TED) onboard NOAA-18. The gray shades indicate IPA zone.

We applied a second-order Savitzky-Golay smoothing filter to define the background magnetic field, and extracted transverse (\hat{x} : toward outer L-shells, \hat{y} : toward magnetic east) and compressional (\hat{z} : parallel to the ambient magnetic field) electromagnetic pulsations in local field-aligned coordinates. To estimate the satellite footprints and the equatorial gyrofrequencies of ions, we used the T96 model (Tsyganenko, 1995) combined with the International Geomagnetic Reference Field (IGRF) model. The Altitude Adjusted Corrected Geomagnetic (AACGM) coordinate system (Shepherd, 2014) is used for ionospheric and ground locations.

3. Observations

In this section, we show our observational results for three events. For each event, we first introduce the Pc1 wave observations on the ground and compare them to auroral emissions at 100–120 km, typical altitudes of auroral emission. Subsequently, we observe the ionospheric F-layer using Swarm data at altitudes of 400–500 km to examine the ionospheric responses to the proton precipitation. Finally, we approach higher altitudes of ~800 km to investigate the proton precipitation by data from the NOAA satellites.

3.1. Event 1: March 19, 2020

During a substorm period (onset time at ~00:30 UT) with a maximum AE index of ~800 nT at ~00:45 UT, IPDP-type Pc1 waves (~0.2–1.2 Hz) were continuously observed from ~00:30 UT to 01:50 UT at both the northern and southern hemispheres in the pre-midnight sector. Figures 1a and 1b show wave spectrograms of horizontal magnetic pulsations measured at Kapuskasing (KAP, $L \sim 3.7$, $MLAT = 58.4^\circ$, $MLT = 18.1$ at 1 UT) at south of Hudson Bay in Canada and at King Sejong Station (KSS, $L \sim 2.3$, $MLAT: -48.6^\circ$, $MLT = 20.8$ at 1 UT) in Antarctica, respectively. The two stations are not exactly conjugate to each other. Still, spectral shapes of the waves are identical, indicating that ground Pc1 waves are EMIC waves that propagated from the equatorial magnetospheric source region to both hemispheres. The overall wave intensity is stronger at KAP than at KSS, and the bandwidth is also larger at KAP than at KSS, which implies that KSS observed ducted Pc1 waves from the wave injection region at higher latitude.

Figures 1c and 1d show north-south keograms (cross-section) of 557.7-nm and 486.1-nm auroral intensities (units of kilo-Rayleigh and Rayleigh) mapped onto an altitude of 100 km, respectively. The maximum intensities over the longitudinal range between 270° and 285° are shown for each latitude for each time. We note that it was important to adjust the color scales when presenting auroral emission on a 2-D image. By reducing the maximum threshold of the color scales, auroral emissions look brighter, and the isolated structure

may be buried in the background. On the other hand, increasing the maximum threshold, auroral emissions look darken, but the isolated spot is clearly visible. Therefore, in the present study, the color scale of auroral images was optimized to present IPA. During the Pc1 wave activity, the concurrent auroral emissions at both auroral oval and subauroral latitudes are detected. Note that auroral images were available only from 00:50 UT, while Pc1 waves were observed on the ground from an earlier time. The keogram of 557.7-nm shows that strong auroral emissions above 54° GLAT (63° MLAT) were continuously detected from 00:50 UT, and it extended both poleward and equatorward from 01:06 UT (the leftmost red dashed line) when strong broadband Pc1 waves suddenly occurred. The strong-broad auroral emissions in 486.1-nm without those in 557.7-nm between 00:50 UT and 01:03 UT are due to twilight: hydrogen is dominant at higher altitude while lower altitude is mainly filled with oxygen which means sunlight is more effective in generating 486.1 nm emission at higher altitudes. A detached auroral arc appeared from 01:06 UT at 54° GLAT, and an additional arc appeared when the second broadband Pc1 waves occurred at 01:23 UT at 52° GLAT (the middle red dashed line). These two arcs are also detected at 486.1-nm and moved toward lower latitudes as the wave frequency increased, and the main auroral arc faded away from 01:42 UT when Pc1 waves below 0.5 Hz weakened (the rightmost red dashed line), and another arc reached 50° GLAT and disappeared with the Pc1 waves (Figure 1c). Auroral emissions above 54° GLAT were still present, but their intensity diminished after lower-frequency parts of the Pc1 wave disappeared. The region above 54° GLAT is typically considered as the auroral oval, in which emissions seem to be mixed with those caused by precipitating electrons coming from the plasma sheet, that is, are related to both Pc1 waves and substorm injection (e.g., Zhou et al., 2021). Hence, in this event, we mainly focus on the emissions at latitudes below 54° GLAT, and we regard this region as a pure IPA zone, which is consistent with isolated auroral structures shown by previous studies (e.g., Sakaguchi et al., 2007, 2008, 2016).

Figures 1e and 1i show auroral images at 01:35:47 UT and 01:41:28 UT (exposure start times), respectively. For the 486.1-nm auroral image, see Figure S1. Several separated auroral regions were visible over Hudson Bay, and an IPA zone was clearly seen below 54° GLAT (63° MLAT, the white dashed line). The time-lapse animation of the auroral emission and Pc1 wave spectrogram is shown in Movie S1. The temporal correspondence between the Pc1 and IPA intensifications at 01:06 UT and 01:23 UT was clearly seen in this movie.

In the following, the Swarm observations in the ionospheric F-layer are described. Figure 1f shows the wave spectrogram of δB_x observed by Swarm-B during a time interval between 01:33 UT and 01:45 UT. Wave spectrograms of the full triaxial-magnetic field residuals with ground Pc1 waves are plotted in Figures S2a–S2d. The white dashed curves indicate equatorial gyrofrequencies of hydrogen, helium, and oxygen estimated based on the IGRF and T96 magnetic field model. During strong Pc1 wave activity on the ground, footprints of Swarm-B crossed over the IPA zone at around 01:36 UT (see Figure 1e), during which strong broadband transverse pulsations were observed (see also δB_y in Figure S2c).

The protruded helium-band transverse Pc1 waves at ~ 0.2 –1.0 Hz corresponding to the ground Pc1 wave emerged at the equatorial boundary of broadband pulsations after 01:36:20 UT (red vertical solid line in Figures 1f and 1g). Note that Pc1 wave band in δB_x and ground was spectrally narrower than that in δB_y (Figures S2a–S2c). Thus, we regard the broader band pulsations in δB_y as not being associated with EMIC waves. Swarm-B observed weak compressional (δB_z) pulsations (Figure S2d), which indicates that partial mode conversion occurred. Note that pulsations after 01:37 UT are beyond the scope of this study because they were far from the subauroral latitude, a putative injection region of the Pc1 wave.

Figure 1h shows the auroral intensity (black line) at the corresponding Swarm-B footprints on the image taken at 01:35:47 UT, plasma density (n_p , red line), and low-pass-filtered (20-s) FAC (blue line) measured by Swarm-B between 01:35 UT and 01:37 UT. Wider intervals of n_p and FAC are plotted in Figure S2g. During this event, Swarm-B passed over the plasma trough, where the plasma concentration is lower than immediately poleward and equatorward (Rodger et al., 1992). Three main peaks of auroral intensity of ~ 1.0 –1.3 kR were clearly seen at 01:35:20, 01:35:40 UT (substorm associated), and 01:36:05 UT, as reflected in Figure 1e. Inside the IPA spot, shaded by gray color, Swarm-B detected two local peaks of n_p by a factor of up to 2 relative to the ambient plasma and upward/downward FACs of $\sim \pm 1 \mu A m^{-2}$.

Event 2. 12 September 2018

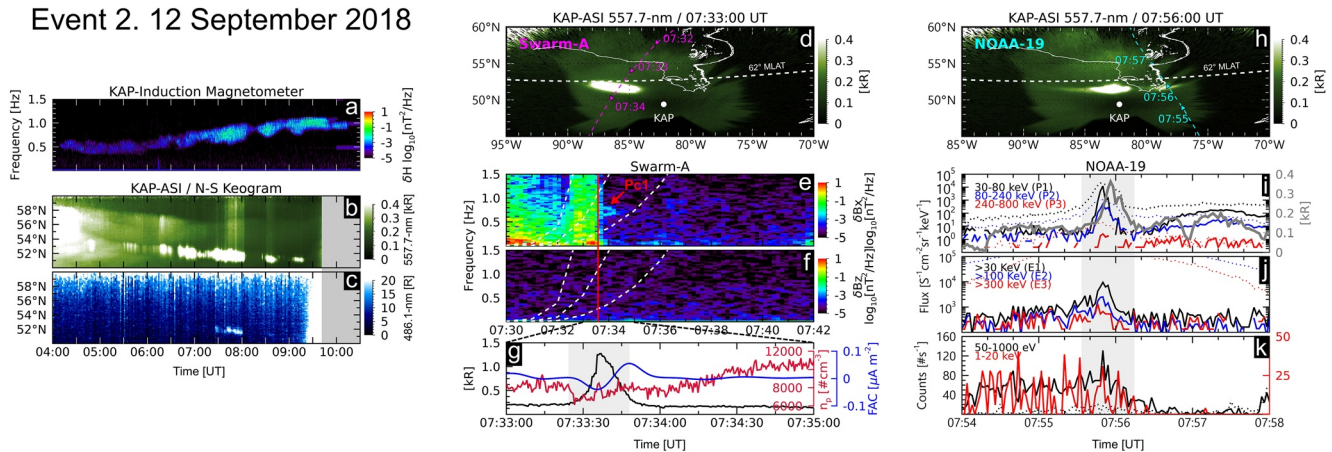


Figure 2. Stack plot of multi-instrument observations for Event 2. (a) Wave spectrogram of horizontal magnetic pulsation observed at Kapuskasing (KAP). (b and c) North-south keogram of 557.7-nm and 486.1-nm auroral emission (d and h) Auroral images at 07:34:30 UT and 07:56:00 UT with satellite footprints. The white dashed lines indicate 62° MLAT (e and f) Wave spectrograms of δB_x and δB_z observed by Swarm-A. The white dashed curves indicate equatorial gyrofrequencies for hydrogen, helium, and oxygen from left to right, while the red solid line indicates when Swarm-A crosses the equatorward boundary of broadband pulsations. (g) Auroral intensity (black), plasma density n_p (red), and field-aligned current (FAC) measured by Swarm-A. (i) Proton and (j) electron fluxes measured by Medium Energy Proton and Electron Detector (MEPED) and (k) proton count rates from Total Energy Detector (TED) onboard NOAA-19.

In the following, the particle detection data from NOAA-18 are described. Figures 1j and 1k show fluxes of energetic protons (30–800 keV, superposed with auroral intensity) and electrons (>30 keV) detected by the MEPED instrument. Solid lines indicate precipitating particles, and dashed lines indicate trapped (mirroring) particles. While the footprint of NOAA-18 crossed over the IPA zone (Figure 1i and gray shade), isolated energetic proton precipitations were detected between 01:41:35 UT and 01:42:00 UT at all energy channels. The fluxes of 30–240 keV protons (black and blue lines) were much larger than those of higher energies (240–800 keV protons, red line). Electron precipitations were also detected for all energy channels. Note, however, that electron counts for <700 keV can be contaminated by high-energy protons due to the sensitive response by the electron detector to 80–2,500 keV protons (Yando et al., 2011). Also, the peak electron flux at >30 keV with very low fluxes of >100 keV implies that most detections were lower-energy electrons with less than 100 keV or they were possibly contaminated by 200–2,700 keV protons (Evans & Greer, 2004). Since EMIC waves are known to interact typically with relativistic electrons with energies higher than a few hundred keV (e.g., Capannolo et al., 2021; Hendry et al., 2017; Miyoshi et al., 2008), we checked relativistic electron precipitation from the >6,900 keV proton channel (P6), which also responded to >700 keV electrons (E4 channel), but no relativistic electrons were detected during this event (Figure S3c). According to Fu et al. (2018), EMIC waves can also interact with <100 keV electrons when the ambient plasma density and frequency are high. Unfortunately, none of magnetospheric satellites were in the possible source region of the EMIC waves and no precipitating electrons for 50 eV–20 keV were detected by TED instrument (not shown here). Hence, we regard the precipitating particles observed by NOAA-18 as being dominated more by energetic protons than electrons. Figure 1l shows proton count rates for low energies of 50–1,000 eV (black line) and 1–20 keV (red line) detected by the TED. Increase of precipitating protons of energies between 1 and 20 keV was clearly seen inside the IPA spot, but that of low-energy protons (50–1,000 eV) was not detected.

3.2. Event 2: September 12, 2018

During a substorm recovery phase (onset time at ~02:20 UT) with a maximum AE index of ~250 nT at ~02:40 UT, IPDP-type Pc1 waves (~0.3–1.1 Hz) were observed from 04:10 UT to 10:15 UT at KAP in the dawn sector (MLT = 1.8 at 07 UT), as shown in Figure 2a. Before Pc1 wave activity, widespread auroral emissions associated with a substorm were covering the nominal auroral and subauroral latitudes on 100 km altitude. The IPA emerged over the western sky among substorm auroral emissions from 04:45 UT onwards (see Movie S2). Figures 2b and 2c show a north-south keogram of 557.7-nm and 486.1-nm auroral emissions, and a distinct IPA temporarily presented up between 04:45 UT and 04:55 UT at latitudes below

$\sim 54^\circ$ in 557.7-nm. From 05:30 UT, a weak, narrow IPA appeared again, and it became stronger when the Pc1 wave intensified at 06:15 UT. At this moment, strong auroral emission in the auroral oval ($>54^\circ$) was also observed with Pi2 pulsations (<0.2 Hz) associated with the substorm. IPA moved equatorward as the Pc1 wave frequency increased, and its brightness was modulated according to the Pc1 wave intensity, similarly to Event 1. The IPA was not observed after 09:20 UT while the Pc1 wave lasted until 10:15 UT. The strong-broad auroral emissions in 486.1-nm after 09:20 UT are because of twilight as for Event 1. Figures 2d and 2h show auroral images taken at 07:34:30 UT and 07:56:00 UT, respectively. For the 486.1-nm auroral image, see Figure S4. A clean IPA zone was seen below 53° (62° MLAT, white dashed line), and it azimuthally extended as time passed (see also Movie S2).

In the following, the Swarm observations are described. During this event, Swarm-A was flying inside a plasma trough (Figure S5g) in the southern hemisphere and observed broadband transverse magnetic spectra (Figures 2e and S5c) while its conjugate footprint in the northern hemisphere crossed over the IPA zone between $\sim 07:33$ UT and 07:34 UT (Figure 2d). The protruded narrow helium-band transverse Pc1 waves coinciding with ground Pc1 waves (0.6–0.9 Hz) began to emerge after 07:33:35 UT (red vertical solid line in Figure 2e). We also enlarge the IPA crossing time in Figure 2g and compared the auroral intensity, extracted from the image taken at 07:33:00 UT, with Swarm-A observations. A peak of auroral intensity was clearly seen, as reflected in Figure 2d, and it reached up to 1.3 kR. Swarm-A detected plasma density decrease when it entered the IPA zone at 07:33:25 UT and then it detected a localized n_p enhancement at central IPA at 07:33:36 UT, by a factor of up to 1.3. The upward/downward FACs of $\sim \pm 0.05 \mu A m^{-2}$ were also detected inside IPA zone and the density peak was surrounded by a broader density decrease (07:33:25–07:33:45 UT), which was in turn collocated with downward FAC. We discuss this observation further in Section 4.

At 800 km, NOAA-19 crossed over the eastern edge of the IPA at around 07:56 UT (Figure 2h), and MEPED detected precipitating protons and electrons at all energy channels (Figures 2i and 2j), similarly to Event 1. Relativistic electron precipitations were not detected by the E4 channel (Figure S6c) and no electrons were detected for 50 eV–20 keV (now shown here). Hence, we also suggest that the precipitating particles of this event over IPA zone are dominated by d protons as for Event 1. TED observations in Figure 2k show that the count rate of 50–1,000 eV protons (black) was very low, but had a peak-like structure at the IPA zone. Precipitating protons at 1–20 keV (red) were also seen, but its count rate was not much larger than the background values.

3.3. Event 3: April 2, 2017

The third event occurred during a quiet period (AE < 50 nT) but right after a substorm recovery phase. IP-DP-type Pc1 waves (0.3–1.2 Hz) were observed between 09:00 UT and 12:00 UT at Gakona (GAK, $L = \sim 4.8$, MLAT = 63.1° , MLT = 0.2 at 11 UT) observatory in Alaska (see Movie S3, longer period of wave spectrogram), during which an IPA was also observed. Figures 3a–3c show Pc1 wave activity and the auroral keograms between 11:00 UT and 12:00 UT. Note that we mapped aurora images onto an altitude of 120 km which best matches between IPA and satellite's footprints. Even though we see a short period of IPA (images available from 11:10 UT), its variations show close correspondence with Pc1 wave activity such that the intensity and latitudinal width of the IPA varied with the Pc1 wave intensity and bandwidth as the previous events showed. Figure 3d shows the auroral image taken at 11:10 UT (see Figure S7 for 486.1-nm). A stretched IPA in the east-west direction below 62° MLAT (white dashed line) was clearly seen over south Alaska. The full animation of the auroral emissions compared with the Pc1 wave activity is shown in Movie S3.

Similar to the two previous events, Swarm-A flew over the plasma trough (Figure S8g) and observed strong broadband transverse magnetic spectra (Figures 3e, S8b and S8c) while its footprint crossed over the IPA zone between 10:48 UT and 10:49 UT (Figure 3d). We assume that the IPA actually existed when the Swarm-A passed over Alaska (10:49 UT), slightly before the ASI operation, because Pc1 waves were continuously detected during that period (see Movie S3). The narrow helium-band transverse Pc1 waves coincided with ground Pc1 waves (0.3–0.9 Hz) around the equatorward boundary of broadband pulsations before 10:48:05 UT (red solid line in Figure 3e). We also compared the auroral intensity from the image at 11:10:00 UT to Swarm observations in Figure 3g. The localized peak in the n_p , by a factor of 2 relative to ambient plasma, and upward/downward FAC of $\sim \pm 0.4 A m^{-2}$ were clearly seen inside the IPA spot.

Event 3. 2 April 2017

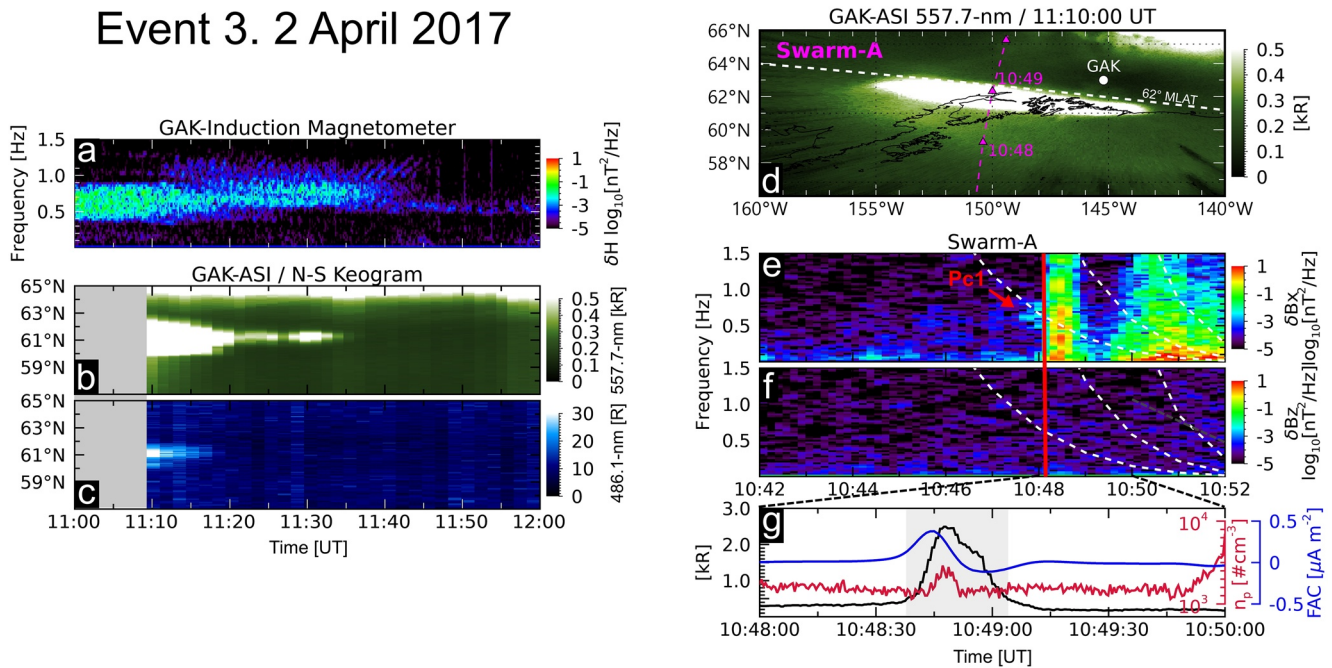


Figure 3. Stack plot of multi-instrument observations for Event 3. (a) Wave spectrogram of horizontal magnetic pulsation observed at GAK (b and c) North-south keogram of 557.7-nm and 486.1-nm auroral emission. (d) Auroral image at 11:10:00 UT with satellite footprints. The white dashed lines indicate 62° MLAT (e and f) Wave spectrograms of δB_x and δB_z observed by Swarm-A. The white dashed curves indicate equatorial gyrofrequencies for hydrogen, helium, and oxygen from right to left, while the red solid line indicates when Swarm-A crosses the equatorward boundary of broadband pulsations. (g) Auroral intensity (black), plasma density n_p (red), and field-aligned current (FAC) measured by Swarm-A.

4. Discussion and Conclusions

We showed changes of ionospheric plasma and FAC over IPAs associated with EMIC Pc1 waves. All the observational results clearly demonstrated that IPDP-type EMICs precipitated energetic protons, creating an IPA at subauroral latitudes. In the ionospheric F-layer, Swarm showed that EMIC-driven proton precipitation caused localized plasma density enhancements, which are embedded in a wider region of very low plasma density in the trough, and FAC structures accompanied by broadband transverse magnetic spectra.

Typically, strong broadband transverse magnetic spectra are observed over the auroral oval due to magnetic field fluctuations (Kim et al., 2018; Park et al., 2013) induced by Region 1 and 2 FACs, whose major contributor is electrons bouncing between plasma sheet and ionosphere. The present study, however, suggests that the FACs over the IPA zone at subauroral latitudes are not the nominal sheet currents related to the auroral oval, but FACs induced mostly by proton precipitation as observed by the NOAA satellites.

The latitudinal width of the broadband transverse magnetic spectra (or FAC and proton precipitation), and that of the IPA may not perfectly fit, as seen in the events discussed in our study. The reason is that the secondary electrons after primary ionization may contribute to auroral emissions around the ionization region, and not all particles generating detectable FACs at the F-layer reach the E-layer. Davidson (1965), using a Monte Carlo method, showed that the E-region is primarily impacted by proton precipitation but the proton's energy deposition starts in the F-region (Figure 6 in Davidson, 1965). The author also found that the repeated charge exchange and electron stripping process transport the particles up to ~ 300 km from the incident region of proton precipitation (see Figures 1 and 6 in Davidson, 1965). According to the 3-D Monte Carlo model calculation from Fang et al., 2004, incident proton beams are dispersed in the altitude of ~ 250 – 450 km, where the first few charge exchange is expected, and they cause wider auroral emissions at altitudes between ~ 120 and 250 km. Hence, the latitudinal width of the IPA may or may not be greater than that of the broadband transverse magnetic spectra. However, all events showed that broadband spectra and FACs were certainly seen over the IPA spots.

The protruded transverse (narrow-band) Pc1 waves observed from the equatorward boundary of the broad-band spectra may imply equatorward/inward oblique propagation of the EMIC waves from the magnetospheric source. Typically, EMIC waves propagate along the magnetic field from the source region, and they can reach ionosphere and ground via polarization reversal (left-to-right handed) at the crossover location and mode conversion (e.g., Johnson et al., 1989; Johnson & Cheng, 1999). During the propagation, wave normal angle can become more oblique and polarization changes from left to linear as waves propagate to higher latitude due to wave refraction by the magnetic gradient and curvature (e.g., Chen et al., 2014; Kim & Johnson, 2016). Kim and Johnson, (2016) also demonstrated that larger normal angle waves can propagate toward smaller L-shell although they calculated the raypath up to $L \sim 6$ (Figure 4 in Kim & Johnson, 2016). Recently, Toledo-Redondo et al. (2021) showed EMIC wave can also be generated at oblique angles when source region consists of a small amount of heavy ions and a large amount of cold protons.

We estimated wave normal angle and polarization in Figures S2e, S2f, S5e, S5f, S8e, and S8f, based on the method by Bortnik et al. (2007). Wave normal angles of narrow-band Pc1 wave at Event 1 and Event 2 seem to suggest weakly oblique propagation (blue and white colors in Figures S2e and S5e) although the Pc1 wave regions are not clearly distinguished from the background. Event 3 shows partially field-aligned wave normal (red), but they are mixed with oblique direction (blue) (Figure S8e). The linear (white) and right-handed (blue) polarizations at Pc1 wave (Figures S2f, S5f, and S8f) support that the EMIC waves propagated from the source region via polarization reversal or change.

Resonance conditions between wave and particle depend on the dispersion relation, which is controlled by the ambient plasma density and ion composition ratio (e.g., Denton et al., 2015; Miyoshi et al., 2019). Hence, the different plasma properties in the wave source region may contribute to the localized proton precipitation, that is, the isolated structure of proton auroras, while changes of wave normal angle from the magnetosphere to the ionosphere can also contribute to the different spatial size between Pc1 wave and IPA. Additional data sets from the source regions, however, are needed to elucidate the wave properties and resonance conditions.

These events showed localized plasma density enhancement in the F-layer over the IPA spot, where peaks in plasma density and the IPA generally coincide (clearly seen in Figures 1h and 3g, while only weakly identifiable in Figure 2g). Typically, energetic electrons and protons ionize neutrals in the E-layer, but our observations showed that the energetic protons also contributed to the ionization in the topside F-layer. According to a model calculation, energetic protons can ionize neutrals at an altitude of >400 km with a rate of up to $10^3 \text{ cm}^{-3}\text{s}^{-1}$ during a geomagnetically active period (e.g., Figure 7 in Fang et al., 2013). Fang et al., (2013) also presented that the higher-energy particles are more effective in causing secondary ionization than lower-energy particles. Fujii et al. (2009), using the European Incoherent Scatter (EISCAT) radar, a proton imager and an ASI, showed upward FAC (electron precipitation) causing thin auroral arc is accompanied by neighboring ionospheric electron density depletion through evacuation process, while widely downward FAC (proton precipitation) generating proton aurora causes electron density increases accompanied by field-aligned and intense perpendicular electric field. Even though they analyzed only one event and did not show the trigger of proton precipitation, their result seems to be consistent with our study that the density enhancement was caused by impact ionization. Furthermore, the larger density increases for the strong IPAs (Events 1 and 3, a factor of 2) than for the weaker IPA (Event 2, a factor of 1.3) also support the idea that the localized plasma density enhancement may result from primary/secondary impact ionization by proton precipitation. The broader density depletion surrounding the peak (07:33:25–07:33:45 UT in Figure 2g) can be interpreted as follows. The collocated downward FAC can expedite electron evacuation and compete with the proton-induced plasma production (e.g., Fujii et al., 2009). This effect competes with the proton-induced ionization (i.e., IPA) to determine the F-region ionospheric density. At the center of the IPA, where proton precipitation would be intense, it can dominate the plasma generation while at the IPA borders other effects, such as downward FAC and electron evacuation, can play an important role in controlling the F-region density structure. Quantitative modeling combined with observations is required to fully address the relative contribution of EMIC-driven proton precipitations to the density variation in the topside ionosphere.

It has been known that other types of detached auroral arcs, such as SAR (stable auroral red) arcs (e.g., Hong et al., 2020; Inaba et al., 2020, 2021) and STEVE (Strong Thermal Emission Velocity Enhancement)

(e.g., Archer et al., 2019) are accompanied by ionospheric irregularities with local density enhancements (SAR arc) and depletions (STEVE) in the auroral regions. Our study also showed that an IPA event is accompanied by localized plasma density enhancements in the plasma trough. Hence, it is worth investigating the statistical ionospheric response to IPAs based on more events and additional data sets, including magnetospheric satellites. In conclusion, our observations demonstrated that energetic proton precipitation driven by EMIC waves contributes to the energy transfer from the magnetosphere to the ionosphere.

Data Availability Statement

The PWING ASI and induction magnetometer data are distributed from the ERG-Science Center (ASI: <https://ergsc.isee.nagoya-u.ac.jp/data/ergsc/ground/camera/omti/asi/>, Induction magnetometer: <https://ergsc.isee.nagoya-u.ac.jp/data/ergsc/ground/geomag/isee/induction/>) operated by ISAS/JAXA and ISEE/Nagoya University (Miyoshi et al., 2018). The induction magnetometer data set recorded at the KSS is provided by KOPRI (lead institute, South Korea) and can be downloaded at <http://mir1.unh.edu/ULF/cdf/>. The Swarm Vector Field Magnetometer, Langmuir Probe and FAC data were obtained online from <https://swarm-diss.esa.int/>. NOAA POES SEM-2 data were downloaded at <https://satdat.ngdc.noaa.gov/sem/poes/data/>.

Acknowledgments

The authors thank the THEMIS SPEDAS team for their open-source library of data analysis tools (Angelopoulos et al., 2019). This work was supported by a Grant-in-Aid for Scientific Research of Japan Society for the Promotion of Science (15H05815, 16H06286, 20H01955, and 20H01959) and the NASA grants 80NSSC18K1043 and 80NSSC20K1670. Hyunju K. Connor gratefully acknowledges support from the NSF grants, OIA-1920965 and AGS-1928883, the NASA grants, 80NSSC18K1052, and 80NSSC19K0844. Junga Hwang was supported by the project “A Study on the Forecasting Model of Space Radiation and the Improvement of Measuring Equipment,” funded by Korea Foundation of Nuclear Safety. Support for the KSS induction magnetometer was provided by grant PE21020 from the KOPRI. The work of H.-J. Kwon was supported by the Basic Science Research Program through NRF funded by NRF-2020R1C1C1003640.

References

- Angelopoulos, V., Cruce, P., Drozdov, A., Grimes, E. W., Hatzigeorgiu, N., King, D. A., et al. (2019). The Space Physics Environment Data Analysis System (SPEDAS). *Space Science Reviews*, 215, 9. <https://doi.org/10.1007/s11214-018-0576-45>
- Archer, W. E., Gallardo-Lacourt, B., Perry, G. W., St-Maurice, J.-P., Buchert, S. C., & Donovan, E. F. (2019). Steve: The optical signature of intense subauroral ion drifts. *Geophysical Research Letters*, 46, 6279–6286. <https://doi.org/10.1029/2019GL082687>
- Bortnik, J., Cutler, J. W., Dunson, C., & Bleier, T. E. (2007). An automatic wave detection algorithm applied to Pc1 pulsations. *Journal of Geophysical Research*, 112(A4), A04204.
- Capannolo, L., Li, W., Spence, H., Johnson, A. T., Shumko, M., Sample, J., & Klumpar, D. (2021). Energetic electron precipitation observed by FIREBIRD-II potentially driven by EMIC waves: Location, extent, and energy range from a multievent analysis. *Geophysical Research Letters*, 48, e2020GL091564. <https://doi.org/10.1029/2020gl091564>
- Chen, L., Jordanova, V. K., Spasojevic, M., Thorne, R. M., & Horne, R. B. (2014). Electromagnetic ion cyclotron wave modeling during the geospace environment modeling challenge event. *Journal of Geophysical Research: Space Physics*, 119, 2963–2977. <https://doi.org/10.1002/2013JA019595>
- Cornwall, J. M., Coroniti, F. V., & Thorne, R. M. (1970). Turbulent loss of ring current protons. *Journal of Geophysical Research*, 75(25), 4699–4709. <https://doi.org/10.1029/JA075i025p04699>
- Davidson, G. T. (1965). Expected spatial distribution of low energy protons precipitated in the auroral zones. *Journal of Geophysical Research*, 70, 1061–1068. <https://doi.org/10.1029/JZ070i005p01061>
- Denton, R. E., Jordanova, V. K., & Bortnik, J. (2015). Resonance of relativistic electrons with electromagnetic ion cyclotron waves. *Geophysical Research Letters*, 42, 8263–8270. <https://doi.org/10.1002/2015GL064379>
- Erlanson, R. E., & Ukhorskiy, A. J. (2001). Observations of electromagnetic ion cyclotron waves during geomagnetic storms: Wave occurrence and pitch angle scattering. *Journal of Geophysical Research*, 106(A3), 3883–3895. <https://doi.org/10.1029/2000JA000083>
- Evans, D. S., & Greer, M. S. (2004). In *Polar orbiting environmental satellite Space environment monitor-2 instrument descriptions and archive data documentation*: Space Environ. Lab.
- Fang, X., Liemohn, M. W., Kozyra, J. U., & Solomon, S. C. (2004). Quantification of the spreading effect of auroral proton precipitation. *Journal of Geophysical Research*, 109, A04309. <https://doi.org/10.1029/2003JA010119>
- Fang, X., Lummerzheim, D., & Jackman, C. H. (2013). Proton impact ionization and a fast calculation method. *Journal of Geophysical Research Space Physics*, 118, 5369–5378. <https://doi.org/10.1002/jgra.50484>
- Frey, H. U., Haerendel, G., Mende, S. B., Forrester, W. T., Immel, T. J., & Ostgaard, N. (2004). Subauroral morning proton spots (SAMPS) as a result of plasmopause-ring-current interaction. *Journal of Geophysical Research*, 109, A10305. <https://doi.org/10.1029/2004JA010516>
- Fu, S., Ni, B., Lou, Y., Bortnik, J., Ge, Y., Tao, X., et al. (2018). Resonant scattering of near-equatorially mirroring electrons by Landau resonance with H⁺ band EMIC waves. *Geophysical Research Letters*, 45, 873. <https://doi.org/10.1029/2018GL079>
- Fujii, R., Iwata, Y., Oyama, S., Nozawa, S., & Ogawa, Y. (2009). Relations between proton auroras, intense electric field, and ionospheric electron density depletion. *Journal of Geophysical Research*, 114, A09304. <https://doi.org/10.1029/2009JA014319>
- Fuselier, S. A., Gary, S. P., Thomsen, M. F., Clafin, E. S., Hubert, B., Sandel, B. R., & Immel, T. (2004). Generation of transient dayside subauroral proton precipitation. *Journal of Geophysical Research*, 109, A12227. <https://doi.org/10.1029/2004JA010393>
- Hendry, A. T., Rodger, C. J., & Clilverd, M. A. (2017). Evidence of sub-MeV EMIC-driven electron precipitation. *Geophysical Research Letters*, 44, 1210–1218. <https://doi.org/10.1002/2016GL071807>
- Hong, J., Kim, J.-H., Chung, J.-K., Kim, Y. H., Kam, H., Park, J., & Mendillo, M. (2020). Simultaneous observations of SAR arc and its ionospheric response at subauroral conjugate points ($L \approx 2.5$) during the St. Patrick's Day Storm in 2015. *Journal of Geophysical Research: Space Physics*, 125. <https://doi.org/10.1029/2019ja027321>
- Immel, T. J., Mende, S. B., Frey, H. U., Peticolas, L. M., Carlson, C. W., Gerard, J.-C., et al. (2002). Precipitation of auroral protons in detached arcs. *Geophysical Research Letters*, 29(11), 1519. <https://doi.org/10.1029/2001GL013847>
- Inaba, Y., Shiokawa, K., Oyama, S., Otsuka, Y., Connors, M., Schofield, I., et al. (2021). Multi-event Analysis of plasma and field variations in Source of Stable Auroral Red (SAR) arcs in inner magnetosphere during non-storm-time substorms. *Journal of Geophysical Research*, 125. <https://doi.org/10.1029/2020JA029081>

- Inaba, Y., Shiokawa, K., Oyama, S., Otsuka, Y., Oksanen, A., Shinbori, A., et al. (2020). Plasma and field observations in the magnetospheric source region of a stable auroral red (SAR) arc by the Arase satellite on 28 March 2017. *Journal of Geophysical Research: Space Physics*, *125*. <https://doi.org/10.1029/2020JA028068>
- Johnson, J. R., Chang, G. B., Crew, B., & Andre, M. (1989). Equatorially generated ULF waves as a source for the turbulence associated with ion conics. *Geophysical Research Letters*, *16*, 1469–1472. <https://doi.org/10.1029/GL016i012p01469>
- Johnson, J. R., & Cheng, C. Z. (1999). Can ion cyclotron waves propagate to the ground? *Geophysical Research Letters*, *26*, 671–674.
- Jordanova, V. K., Farrugia, C. J., Thorne, R. M., Khazanov, G. V., Reeves, G. D., & Thomsen, M. F. (2001). Modeling ring current proton precipitation by electromagnetic ion cyclotron waves during the May 14–16, 1997, storm. *Journal of Geophysical Research*, *106*, 7–22. <https://doi.org/10.1029/2000ja002008>
- Kim, E. H., & Johnson, J. R. (2016). Full-wave modeling of EMIC waves near the He⁺ gyrofrequency. *Geophysical Research Letters*, *43*(1), 13–21. <https://doi.org/10.1002/2015GL066978>
- Kim, H., Hwang, J., Park, J., Bortnik, J., & Lee, J. (2018). Global characteristics of electromagnetic ion cyclotron waves deduced from Swarm satellites. *Journal of Geophysical Research: Space Physics*, *123*, 1325–1336. <https://doi.org/10.1002/2017JA024888>
- Miyoshi, Y., Hori, T., Shoji, M., Teramoto, M., Chang, T.-F., Segawa, T., et al. (2018). The ERG science center. *Earth Planets and Space*, *70*, 96. <https://doi.org/10.1186/s40623-018-0867-8>
- Miyoshi, Y., Matsuda, S., Kurita, S., Nomura, K., Keika, K., Shoji, M., et al. (2019). EMIC waves converted from equatorial noise due to M/Q=2 ions in the plasmapshere: Observations from Van Allen Probes and Arase. *Geophysical Research Letters*, *46*. <https://doi.org/10.1029/2019GL083024>
- Miyoshi, Y., Sakaguchi, K., Shiokawa, K., Evans, D., Albert, J., Connors, M., & Jordanova, V. (2008). Precipitation of radiation belt electrons by EMIC waves, observed from ground and space. *Geophysical Research Letters*, *35*, L23101. <https://doi.org/10.1029/2008GL035727>
- Nakamura, K., Shiokawa, K., Otsuka, Y., Shinbori, A., Miyoshi, Y., Connors, M., et al. (2021). Simultaneous observation of two isolated proton auroras at subauroral latitudes by a highly sensitive all-sky camera and Van Allen Probes. *Journal of Geophysical Research: Space Physics*, *126*, e2020JA029078. <https://doi.org/10.1029/2020JA029078>
- Nomura, R., Shiokawa, K., Omura, Y., Ebihara, Y., Miyoshi, Y., Sakaguchi, K., et al. (2016). Pulsating proton aurora caused by rising tone Pc1 waves. *Journal of Geophysical Research: Space Physics*, *121*, 1608–1618. <https://doi.org/10.1002/2015JA021681>
- Ozaki, M., Shiokawa, K., Miyoshi, Y., Kataoka, R., Connors, M., Inoue, T., et al. (2018). Discovery of 1 Hz range modulation of isolated proton aurora at subauroral latitudes. *Geophysical Research Letters*, *45*(3), 1209–1217. <https://doi.org/10.1002/2017GL076486>
- Park, J., Lühr, H., & Rauberg, J. (2013). Global characteristics of Pc1 magnetic pulsations during solar cycle 23 deduced from CHAMP data. *Annales de Geophysique*, *31*(9), 1507–1520. <https://doi.org/10.5194/angeo-31-1507-2013>
- Ritter, P., Lühr, H., & Rauberg, J. (2013). Determining field-aligned currents with the Swarm constellation mission. *Earth Planets and Space*, *65*, 9–1294. <https://doi.org/10.5047/eps.2013.09.006>
- Rodger, A., Moffett, R., & Quegan, S. (1992). The role of ion drift in the formation of ionisation troughs in the mid- and high-latitude ionosphere: A review. *Journal of Atmospheric and Terrestrial Physics*, *54*(1), 1–30. [https://doi.org/10.1016/0021-9169\(92\)90082-V](https://doi.org/10.1016/0021-9169(92)90082-V)
- Sakaguchi, K., Shiokawa, K., Ieda, A., Miyoshi, Y., Otsuka, Y., Ogawa, T., et al. (2007). Simultaneous ground and satellite observations of an isolated proton arc at subauroral latitudes. *Journal of Geophysical Research*, *112*(A4), A04202. <https://doi.org/10.1029/2006ja012135>
- Sakaguchi, K., Shiokawa, K., Miyoshi, Y., & Connors, M. (2016). Isolated proton aurora and Pc1/EMIC waves at subauroral latitudes. In Y. Zhang, & L. J. Paxton (Eds.), *Auroral dynamics and Space weather, geophysical monograph 215* (1st ed., pp. 59–70). John Wiley & Sons, Inc. <https://doi.org/10.1002/9781118978719.ch5>
- Sakaguchi, K., Shiokawa, K., Miyoshi, Y., Otsuka, Y., Ogawa, T., Asamura, K., & Connors, M. (2008). Simultaneous appearance of isolated auroral arcs and Pc 1 geomagnetic pulsations at subauroral latitudes. *Journal of Geophysical Research*, *113*, A05201. <https://doi.org/10.1029/2007JA012888>
- Shepherd, S. G. (2014). Altitude-adjusted corrected geomagnetic coordinates: Definition and functional approximations. *Journal of Geophysical Research*, *119*(7), 521. <https://doi.org/10.1002/2014JA020264>
- Shiokawa, K., Katoh, Y., Hamaguchi, Y., Yamamoto, Y., Adachi, T., Ozaki, M., et al. (2017). Ground-based instruments of the PWING project to investigate dynamics of the inner magnetosphere at subauroral latitudes as a part of the ERG-ground coordinated observation network. *Earth Planets and Space*, *69*(160). <https://doi.org/10.1186/s40623-017-0745-9>
- Spasojevic, M., Frey, H. U., Thomsen, M. F., Fuselier, S. A., Gary, S. P., Sandel, B. R., & Inan, U. S. (2004). The link between a detached subauroral proton arc and a plasmaspheric plume. *Geophysical Research Letters*, *31*, L04803. <https://doi.org/10.1029/2003GL018389>
- Toledo-Redondo, M., Lee, J. H., Vines, S. K., Turner, D. L., Allen, R. C., André, M. et al. (2021). Kinetic interaction of cold and hot protons with an oblique EMIC wave near the dayside reconnecting magnetopause. *Geophysical Research Letters*, *48*. e2021GL092376. <https://doi.org/10.1029/2021GL092376>
- Tsyganenko, N. A. (1995). Modeling the Earth's magnetospheric magnetic field confined within a realistic magnetopause. *Journal of Geophysical Research*, *100*(A4), 5599–5612. <https://doi.org/10.1029/94ja03193>
- Usanova, M. E., Drozdov, A., Orlova, K., Mann, I. R., Shprits, Y., Robertson, M. T., et al. (2014). Effect of EMIC waves on relativistic and ultra-relativistic electron populations: Ground-based and Van Allen Probes observations. *Geophysical Research Letters*, *41*, 1375–1381. <https://doi.org/10.1002/2013GL059024>
- Yahnin, A. G., & Yahnina, T. A. (2007). Energetic proton precipitation related to ion-cyclotron waves. *Journal of Atmospheric and Solar*, *69*(14), 1690–1706. <https://doi.org/10.1016/j.jastp.2007.02.010>
- Yahnin, A. G., Yahnina, T. A., & Frey, H. U. (2007). Subauroral proton spots visualize the Pc1 source. *Journal of Geophysics Research*, *112*, A10223. <https://doi.org/10.1029/2007JA012501>
- Yahnina, T. A., Yahnin, A. G., Kangas, J., & Manninen, J. (2000). Proton precipitation related to Pc1 pulsations. *Geophysical Research Letters*, *27*(21), 3575–3578. <https://doi.org/10.1029/2000gl003763>
- Yahnina, T. A., Yahnin, A. G., Kangas, J., Manninen, J., Evans, D. S., Demekhov, A. G., et al. (2003). Energetic particle counterparts for geomagnetic pulsations of Pc1 and IPDP types. *Annales Geophysicae*, *21*(12), 2281–2292. <https://doi.org/10.5194/angeo-21-2281-2003>
- Yando, K., Millan, R. M., Green, J. C., & Evans, D. S. (2011). A Monte Carlo simulation of the NOAA POES medium energy proton and Electron detector instrument. *Journal of Geophysics Research*, *116*, A10231. <https://doi.org/10.1029/2011JA016671>
- Zhou, S., Luan, X., Burch, J. L., Yao, Z., Han, D.-S., Tian, C., et al. (2021). A possible mechanism on the detachment between a subauroral proton arc and the auroral oval. *Journal of Geophysical Research: Space Physics*, *126*, e2020JA028493. <https://doi.org/10.1029/2020JA028493>

Erratum

Two changes have been made to this article since it was originally published. In Figure 2h, the position of the white dashed line was drawn at 61° MLAT, while the article mentions 62° MLAT. Figure 2h has been updated. Additionally, in section 3.2, the last sentence of the first paragraph, an instance of 62.5° MLAT has been corrected to 62° MLAT. The present version may be considered the authoritative version of record.